Jocelyn M. Kluger
Department of Mechanical Engineering,
Massachusetts Institute of Technology,
Cambridge, MA 02139
e-mail: jociek@mit.edu

Alexander H. Slocum[1]
Professor
Department of Mechanical Engineering,
Massachusetts Institute of Technology,
Cambridge, MA 02139
e-mail: slocum@mit.edu

Themistoklis P. Sapsis
Department of Mechanical
and Ocean Engineering,
Massachusetts Institute of Technology,
Cambridge, MA 02139
e-mail: sapsis@mit.edu

Ring-Based Stiffening Flexure Applied as a Load Cell With High Resolution and Large Force Range

This paper applies linear elastic theory and Castigliano's first theorem to design nonlinear (stiffening) flexures used as load cells with both large force range and large resolution. Low stiffness at small forces causes high sensitivity, while high stiffness at large forces prevents over-straining. With a standard 0.1 μm deflection sensor, the nonlinear load cell may detect 1% changes in force over five orders of force magnitude. In comparison, a traditional linear load cell functions over only three orders of magnitude. We physically implement the nonlinear flexure as a ring that increasingly contacts rigid surfaces with carefully chosen curvatures as more force is applied. We analytically describe the load cell performance as a function of its geometry. We describe methods for manufacturing the flexure from a monolithic part or multiple parts. We experimentally verify the theory for two load cells with different parameters. [DOI: 10.1115/1.4037243]

1 Introduction

Compliant mechanisms, or flexures, are machine joints that transfer motions and forces without friction, resulting in little wear or backlash and high precision. Most nonlinear compliant mechanism literature concerns nonlinearities due to the material or geometric constraints, and the nonlinearity is not desired but needs to be included in a model. The most common nonlinearities are elastomer and power-law materials that behave linearly for small deflections but weaken at large deflections [1]. Axial stretching and geometric constraints lead to stiffening behavior for large deflections [2]. Typically, the change in stiffness in flexure mechanisms is not as extreme as the change in the mechanism described in this paper. Flexure applications include prosthetics [3], nanopositioning for semiconductor fabrication [4], gyroscope acceleration detection [2], and energy-harvesting devices [5]. This paper focuses on the use of flexures as load cells [6], although the analysis and fabrication methods may be relevant to many other applications.

Load cells are often implemented as S-beams or disks that deform under a force and cause a deflection or strain transducer to send a corresponding electric signal [7]. Load cells themselves have a large set of applications ranging from material strength testing to prosthetic limb sensing [8], monitoring infusion pumps delivering drugs [9], agricultural product sorting [10], and human–robot collision force sensing [11]. Traditional linear load cells can be designed for almost any force capacity from 1.0×10^{-1}–2.5×10^{6} N and withstand 50–500% overload capacity by the use of overstops [7]. Because traditional load cells deform linearly, they have constant force measurement resolution over their entire force range.

There are several challenges for designing a load cell. The load cell should have minimal mass, volume, hysteresis, and parasitic load sensitivity [7]. The most critical challenge is the trade-off between force sensitivity and range: It is desirable to maximize load cell strain or deflection in order to increase the force measurement resolution by the strain or deflection sensor, which typically resolves 14-bits between 0 and its maximum rated measurement [12–14]. Simultaneously, one wants to maximize the load cell's functional force range and protect it from overloading, which requires limiting the strain.

A common approach for overcoming this design challenge is using multiple linear springs with varied stiffnesses in series [10,15,16]. Overload stops prevent the weaker springs from deflecting too far, after which the stiffer springs continue to deflect. Using this approach, Storace and Sette [15] were able to measure weights over a range of 1–30 kg. The device of Chang and Lin [10] uses two linear load cells and has dimensions of $100 \times 100 \times 30$ mm^3. This is about twice the frontal area of a typical 1000 N linear load cell, which is $50 \times 60 \times 12$ mm^3. Challenges with this multiple-spring-and-transducer approach may be that it results in a bulky, expensive, or less reliable load cell compared to a single-spring-and-transducer device.

Our approach for designing a load cell with high force resolution and capacity is to use a nonlinear-stiffening mechanism rather than multiple linear ones [17]. A nonlinear load cell may have a low stiffness at low forces, and therefore, its deflection and strain will be very sensitive to the applied force. When used with a constant-resolution deflection sensor, this allows the load cell to have high force resolution at small forces. High stiffness at large forces protects the load cell from over-straining. The design may be volume compact and inexpensive due to requiring only one nonlinear spring and sensor per device.

This paper describes a nonlinear-stiffening load cell which uses curved beams that increasingly contact surfaces with carefully chosen curvatures as more force is applied, as shown in Fig. 1. We derived the design starting from a nonlinear cantilever-surface spring described by Timosheko [5,18]. This load cell has high resolution (within 1% of the force value) over a large range (five orders of magnitude). An absolute linear encoder senses the nonlinear deflection. This combined flexible element and rigid surface mechanism has minimal hysteresis [6]. In Sec. 2, we develop the force-deflection theory. In Sec. 3, we describe two methods for manufacturing the load cell mechanical components from one monolithic part or multiple parts. In Sec. 4, we describe the load cell performance sensitivity to geometric parameters. In Sec. 5, we experimentally verify the theory for a monolithic and multipart load cell. We describe conclusions in Sec. 6.

[1]Corresponding author.

Contributed by the Design Innovation and Devices of ASME for publication in the Journal of Mechanical Design. Manuscript received September 12, 2016; final manuscript received June 7, 2017; published online August 30, 2017. Assoc. Editor: David Myszka.

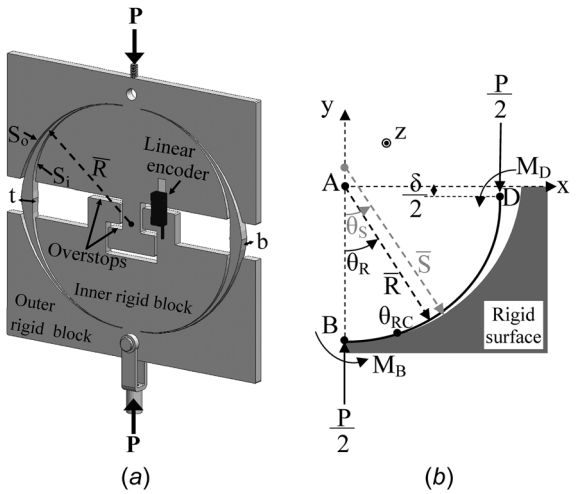

Fig. 1 A nonlinear load cell flexure cut from a flat plate with an applied load *P*: (*a*) entire load cell with a linear encoder and (*b*) free body diagram of one symmetric flexure quadrant for compression mode

2 Theoretical Modeling

We consider the nonlinear ring flexure shown in Fig. 1. The flexure deflects nonlinearly as increasing force causes an increasing length of the ring to wrap along the surface starting from $\theta_R = 0$. As the free length of the ring shortens, the flexure stiffens.

We found that the flexure stiffening rate may be favorably decreased, as described in Sec. 4, when the ring thickness is tapered; that is, the ring thickness symmetrically increases in each quadrant from the root, $\theta_R = 0$ to $\theta_R = \pi/2$ according to

$$t(\theta_R) = t_i + (t_f - t_i)\left(\frac{\theta_R}{\pi/2}\right)^q \tag{1}$$

where t_i is the ring thickness in the flexure plane at $\theta_R = 0$, t_f is the thickness at $\theta_R = \pi/2$, and q is a chosen power parameter. The variable thickness causes variable ring rigidity

$$\mathrm{EI}(\theta_R) = E\frac{b(t(\theta_R))^3}{12} \tag{2}$$

We determine the ring deflection as a function of force, P, in four main steps:

(1) Express the internal loading along the ring as a function of the applied force, P.
(2) Determine the free segment's boundary conditions for each applied force, P. By "boundary conditions," we refer to the two unknown parameters that appear in the strain energy expression: the ring–surface contact angle, $\theta_{\mathrm{RC}}(P)$, and the reaction moment, $M_D(P)$, as labeled in Fig. 1(*b*). θ_{RC} is the coordinate along the ring where the deformed ring stops conforming to the surface shape.
(3) Express the strain energy in the ring as a function of the applied force, P.
(4) Use Castigliano's first theorem to calculate the cumulative ring deflection for increasing force, P.

In our derivation, we consider a compressive loading and use the sign convention shown in Fig. 1(*b*). The tensile loading theory matches the compression theory when the force P is negative-valued, and the surface mean radius is smaller than the ring mean radius, $\overline{S} < \overline{R}$.

We make several simplifying assumptions in our model:

- Transverse shear strain effects are negligible so Euler–Bernoulli beam theory applies [19].
- The flexure deflects only in-plane.
- Once a ring segment wraps around the surface, it conforms to the surface shape and does not lift away from the surface for larger forces.
- A no-slip condition also applies to the ring segment in contact with the surface.
- In this paper, we consider only a surface with a constant radius, $\overline{S}$. Future work may extend the theory for surface curvatures that change with θ_S.

2.1 Internal Loading Along the Ring. First, we describe internal bending moments and forces along the ring. For the ring segment in contact with the surface, $\theta_R < \theta_{\mathrm{RC}}$, the ring curvature changes to match the mean surface curvature

$$\Delta\kappa = \frac{1}{\overline{S}} - \frac{1}{\overline{R}} \tag{3}$$

The mean surface radius, $\overline{S}$, is a theoretical design parameter. The physically fabricated outer surface radius $S_o(\theta_S)$ differs from $\overline{S}$ to account for the tapered ring thickness. $S_o(\theta_S)$ is $\overline{S}$ plus half the ring thickness, $t(\theta_R)$, at the ring location, θ_R, that contacts the surface at θ_S. We find the ring location, θ_R, that contacts a certain surface location, θ_S, by equating the curves' arc lengths

$$\overline{R}\theta_R = \overline{S}\theta_S \tag{4}$$

The physically fabricated outer surface radius is

$$S(\theta_S) = \overline{S} + \frac{t\left(\frac{\overline{S}\theta_S}{\overline{R}}\right)}{2} \tag{5}$$

where the ring thickness is defined in Eq. (1). Subtraction is used instead of addition for the inner surface radius. The load cell nonlinear deflection is symmetric in compression and tension modes if the inner and outer rigid surfaces cause the same magnitude $\Delta\kappa$ as the ring wraps around them.

Along the free ring segment, $\theta_{\mathrm{RC}} < \theta_R < \pi/2$, the internal bending moment is

$$M(\theta_R) = M_D - \frac{P}{2}\overline{R}(1 - \sin(\theta_R)) \tag{6}$$

where M_D is a reaction moment at $\theta_R = \pi/2$, as shown in Fig. 1.

Along the entire ring, the force normal to the ring's cross section is

$$N(\theta_R) = -\frac{P}{2}\sin(\theta_R) \tag{7}$$

The shear force parallel to the cross section is

$$V(\theta_R) = -\frac{P}{2}\cos(\theta_R) \tag{8}$$

2.2 Equations to Determine the Free Ring Segment Boundary Conditions. Next, we determine the contact angle, $\theta_{\mathrm{RC}}(P)$, and reaction moment, $M_D(P)$, for a given force, P. We use Euler–Bernoulli beam theory relating a thin ring's internal moment to the change in curvature

$$M = \mathrm{EI}\Delta\kappa \tag{9}$$

First, we consider $\theta_{\mathrm{RC}}(P)$. For the ring segment in contact with the surface, $\theta_R < \theta_{\mathrm{RC}}$, we assume that the ring curvature changes to match the surface mean curvature. At the contact angle, the ring change in curvature is continuous because the surface does

Table 1 Fabricated load cell parameters

Parameter	Multipart load cell	Monolithic load cell
Ring mean radius, $\overline{R}$ (mm)	74.67	80.00
Inner surface mean radius, $\overline{S}_i$ (mm)	70.00	77.00
Outer surface mean radius, $\overline{S}_o$ (mm)	80.00	83.24
Ring width, b (mm)	12.70	6.35
Ring thickness at root, t_i (mm)	0.508	0.50
Ring thickness at $\theta_R = \pi/2$, t_f (mm)	0.508	10.00
Ring polynomial for thickness variation, q	—	3
Ring material	Blue tempered steel 1095	Aluminum 7075-T651
Ring elastic modulus, E (GPa)	205	72
Ring yield stress (MPa)	1800	420

not impose an applied moment on the ring. We apply Euler–Bernoulli beam theory, Eq. (9), at the contact angle to equate the ring change in the curvature required for surface tangency and the change in the curvature due to the internal moment

$$M(\theta_{\mathrm{RC}}) = \mathrm{EI}(\theta_{\mathrm{RC}})\Delta\kappa(\theta_{\mathrm{RC}}) \tag{10}$$

where $EI(\theta_R)$ is the ring cross section rigidity defined in Eq. (2), $\Delta\kappa(\theta_R)$ is the change in curvature defined in Eq. (3), and $M(\theta_R, M_D, P)$ is the internal moment defined in Eq. (6).

Second, we consider $M_D(P)$. As shown in Fig. 1, the ring cannot rotate about the z axis at point D due to symmetry. Counterclockwise rotation of the ring at point D due to internal loading is

$$\phi_D = \int_0^{\pi/2} \Delta\kappa\,\overline{R}\,\mathrm{d}\theta_R = 0 \tag{11}$$

Substituting Eqs. (3), (6), and (9) into Eq. (11), the rotation at D is

$$\phi_D = \Delta\kappa_S\,\overline{R}\,\theta_{\mathrm{RC}} + \int_{\theta_{\mathrm{RC}}}^{\pi/2} \frac{M(\theta_R, M_D, P)}{\mathrm{EI}(\theta_R)}\overline{R}\,\mathrm{d}\theta_R = 0 \tag{12}$$

We simultaneously solve Eqs. (10) and (12) for $\theta_{\mathrm{RC}}(P)$ and $M_D(P)$ using the numeric solver fsolve in MATLAB for each force, P.

2.3 Complementary Strain Energy in the Ring. Complementary strain energy in the ring is the summation of internal bending, shear, and normal complementary energies [19]

$$U = U_{\mathrm{Bend}} + U_{\mathrm{Shear}} + U_{\mathrm{Normal}} \tag{13}$$

While bending dominates the load cell internal energy for small forces, shear and normal energy become significant as the ring free segment shortens. The complementary bending energy along the entire thin ring is

$$U_{\mathrm{Bend}} = 4\left(\int_0^{\theta_{RC}} \frac{\mathrm{EI}(\Delta\kappa)^2}{2}\overline{R}\,\mathrm{d}\theta_R + \int_{\theta_{\mathrm{RC}}}^{\pi/2} \frac{M^2}{2\mathrm{EI}}\overline{R}\,\mathrm{d}\theta_R\right) \tag{14}$$

The factor of 4 accounts for the four ring quadrants. Complementary energy due to the internal shear force is

$$U_{\mathrm{Shear}} = \int_0^{2\pi} \frac{6V^2}{10GA}\overline{R}\,\mathrm{d}\theta_R \tag{15}$$

where GA is the ring cross section's shear stiffness. Complementary energy due to the normal force is

$$U_{\mathrm{Normal}} = \int_0^{2\pi} \frac{N^2}{2AE}\overline{R}\,\mathrm{d}\theta_R \tag{16}$$

2.4 Castigliano's First Theorem to Determine Deflection. We use Castigliano's first theorem to calculate the cumulative ring deflection as increasing force is applied [19]

$$\delta = \int_0^P \frac{\dfrac{\partial U(F)}{\partial F}}{F}\mathrm{d}F \tag{17}$$

where the complementary strain energy, U, in the ring is defined in Eq. (13).

3 Fabrication Methods

We consider two different load cell designs. We fabricated both load cells using an Omax MicroMAX waterjet machine with the parameters listed in Table 1. The Omax MicroMAX cuts with a near-zero taper [20]. Slight angles in the surface due to a waterjet taper would negatively affect the theory by reducing the amount of ring-surface contact.

The first design is a multipart load cell assembled from two inner blocks, two outer blocks, and two flat spring steel beams bent into rings, all bolted together, as shown in Fig. 2(*a*). The spring steel ring has a constant thickness. The second design is a monolithic load cell, where the blocks and flexible ring are cut from a single sheet of 7071 aluminum, and the ring has a variable thickness along its length (0.5 mm at the flexure root and 10 mm at 90 deg), as shown in Fig. 2(*b*). As shown in Fig. 2(*c*), we cut gaps at the surface roots and inserted curved blocks to extend the surface curve to the root. This was required because the waterjet cannot cut a kerf smaller than 0.4 mm, and for the chosen parameters, the load cell performance is quite sensitive to a gap at the root: with a gap (no block), the load cell deflects with two linear regions due to the ring pivoting about the surface start-point rather than wrapping along the surface starting at the root. This effect was experimentally demonstrated in Kluger et al. [6].

The two designs have different advantages. The main advantage of the multipart load cell is that if the flexure breaks, then only the flexure needs to be replaced, without needing to replace the blocks. If part of the monolithic load cell breaks, then, the entire device needs to be replaced. Another advantage of the multipart load cell is that it is less costly to waterjet: cutting out the ring width from a spring steel sheet requires less precision than cutting out the ring thickness, because the load cell performance is much less sensitive to errors in ring width than errors in ring thickness. A third advantage of the multipart load cell is that the spring steel ring has a higher yield stress than an aluminum ring. Fourth, the minimum ring thickness and minimum difference between ring and surface radii is not limited by the waterjet's kerf and accuracy. Our optimization procedures for the load cell showed that minimizing the difference in ring and surface radii, $\overline{S} - \overline{R}$ increases the load cell range because then the ring undergoes less bending. Minimizing the ring thickness allows the load cell to be sized smaller for a given initial stiffness.

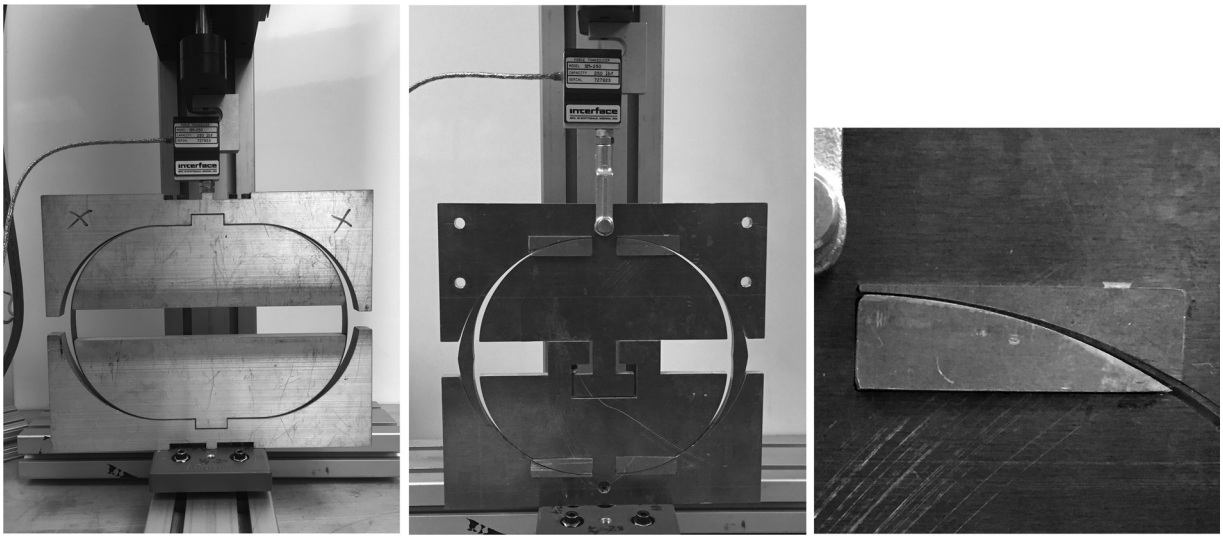

Fig. 2 Fabricated load cells: (*a*) multipart assembled load cell experiment during maximum tension, (*b*) monolithic load cell with tapered ring thickness and root inserts in compression, and (*c*) close-up view of root inserts

The main advantage of the monolithic load cell is that waterjetting the ring thickness allows the ring to have a variable thickness along its length, which allows the ring stiffness to increase with less stress than the shortening mechanism alone. Furthermore, although the monolithic load cell requires root blocks adhered to the surfaces for assembly, it does not require bolts, which risk becoming loose. Finally, the monolithic load cell ring does not have a prestress before any load is applied, as does the multipart load cell fabricated by bending a flat beam into a ring, which limits the maximum compressive force that can be applied to the load cell before yield.

Other features that improve the load cell performance are overstops to prevent overstraining and plates to prevent out-of-plane over-straining. The load cell size can be scaled, as described in Ref. [6].

In terms of performance, both load cell types can be designed with comparable force sensitivity, range, and size, as discussed in Sec. 4.

4 Performance Sensitivity to Parameters

Load cell performance is a tradeoff between flexure stiffness, which limits how finely a deflection sensor may resolve changes in force; and flexure stress, which limits the force capacity.

The load cell stiffness is

$$K = \frac{\partial P}{\partial \delta} \tag{18}$$

If a linear encoder deflection sensor can resolve 0.1 μm deflections and we would like to resolve a force to within 1% its value, then we require the flexure stiffness to remain below

$$K \leq 10^5 P \tag{19}$$

Details on the stiffness limitations for a given force resolution can be found in Ref. [6].

The stress along the ring due to bending is [19]

$$\sigma = \frac{Et\,\Delta\kappa}{2} \tag{20}$$

Equation (20) neglects stress due to the shear and normal forces because we found that these stresses contribute less than 2% to the ring's von Mises equivalent stress.

When the ring is fabricated by bending a flat beam into a circle, the prestress added to the load cell bending stress is

$$\sigma_{\text{Pre}} = \frac{Et}{2\overline{R}} \tag{21}$$

The multipart load cell fabricated from a flat beam and the monolithic load cell can be designed with comparable force sensitivity, range, and size.

While we want the ring to be a weak spring for high sensitivity at small forces, we want it to be a stiff spring to limit bending stress at large forces. As more force is applied to the load cell, two mechanisms cause the ring stiffness to increase: shortening of the free length, and increase in the average thickness of the free length (for the monolithic variable thickness ring only). For the two designs considered in this paper, the variable thickness mechanism allows the ring stiffness to increase with less stress than the shortening mechanism alone, as shown in Figs. 3(*c*) and 3(*d*).

A main limitation for both load cell designs was the minimum allowable ring radius. The multipart load cell radius was limited in order to limit prestress when bending the spring steel beam into a circle. The multipart load cell has a −680 MPa prestress at all points due to bending the flat spring steel beam into a circle, which limits the allowable ring force in compression before yield. On the other hand, the prestress greatly increases the force range in tension, as shown in Fig. 3(*d*). The monolithic load cell radius was limited to decrease the initial stiffness. The load cell's initial stiffness can be decreased (i.e., force sensitivity can be increased) by decreasing the ring thickness or its radius. The monolithic load cell ring thickness was limited by the waterjet kerf and accuracy. For both load cell designs, sensitivity at high forces is not a problem: if the load cell is sensitive at small forces, then its stiffness increases gradually enough so that a constant-deflection–resolution sensor can resolve larger forces with a higher percentage resolution than smaller forces, as shown in Fig. 3(*c*).

Figure 3 illustrates the load cell sensitivity to a fabrication error that increases the ring-surface radius difference, that is, increases the inner surface radius, S_i, or decreases the outer surface, S_o, by 1%, for both load cell designs. Figure 3(*a*) shows that this 1% decrease in surface-ring radius difference decreases the deflection at 1000 N force by 0.69 mm or 20% for the monolithic load cell (0.89 mm or 15% for the multipart load cell). As shown in Fig. 3(*d*), this corresponds to a maximum stress decrease from

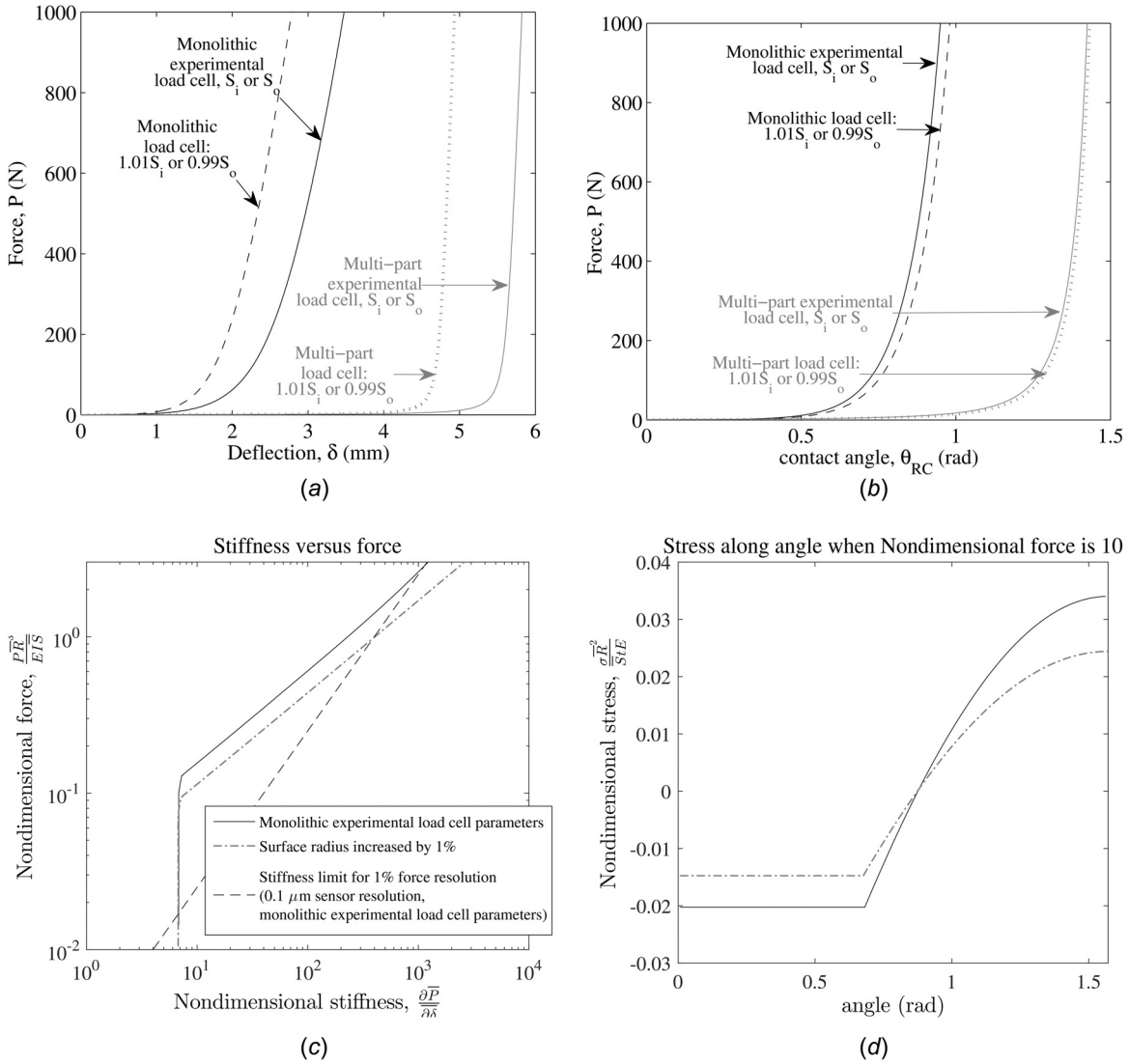

Fig. 3 Load cell performance sensitivity to 1% increase in surface radius: (*a*) force versus deflection, (*b*) force versus contact angle, (*c*) force versus stiffness, and (*d*) stress along the ring inner radius when force $P = 1000$ N. Monolithic load cell: black. Multipart load cell: gray. Experimental parameters: solid line. Inner surface radius S_i increased by 1%: dashed line.

193 MPa to 159 MPa, 18%, for the monolithic load cell (−1363 MPa to −1296 MPa, 5%, for the multipart load cell).

If the reverse fabrication error occurs and the ring-surface radius difference is 1% larger than intended, then overstops will not properly prevent overload. If the monolithic (multipart) load cell is designed for $1.00S_o$ and overstops at 1000 N, but $0.99S_o$ is fabricated, then, the overstops will not engage until 1903 N, a 90% increase (5400 N, a 440% increase), is applied and the stress exceeds 202 MPa, a 4.7% increase (1525 MPa, a 13% increase), not shown. If the monolithic (multipart) load cell is designed for $1.01S_i$ or $0.99S_o$ but $1.00S_i$ or $1.00S_o$ is fabricated, then overstops will stop the load cell deflection at 345 N (9.65 N) rather than 1000 N.

As described above, fabrication errors in the multipart load cell result in larger magnitudes of deflection and force errors than fabrication errors in the monolithic load cell. The multipart load cell's higher sensitivity is due to how its force–deflection curve is initially much flatter and then abruptly approaches a steeper stiffness asymptote than the monolithic load cell.

We note that while the 1% change in surface radius has a significant effect on the load cell's final deflection and stress, it has a small effect on the ring contact angle and stiffness at a given force, as shown in Figs. 3(*b*) and 3(*c*).

In summary, the monolithic load cell has the favorable properties that its stress increases more gradually and its sensitivity to errors is smaller (due to the ring thickness taper), but it has the unfavorable property that its size must be larger (due to radii minimum constraints) than the multipart load cell. Future work will include considering multipart load cells that use surfaces with elliptical shapes rather than circular shapes, as this may reduce the multipart load cell's stress at large forces.

5 Experimental Verification

We performed quasi-static force versus deflection tests to verify the flexure theory described in Sec. 2 and show the effectiveness of the two fabrication methods described in Sec. 3. Figure 4 compares the force versus deflection results to the theory. The two slightly different experimental setups for the multipart and monolithic load cells are shown in Fig. 2. Both tests used an ADMET eXpert 5000 force tester machine with $\pm 5 \times 10^{-5}$ mm resolution that compressed or tensioned the load cell at a rate of 0.05 mm/s,

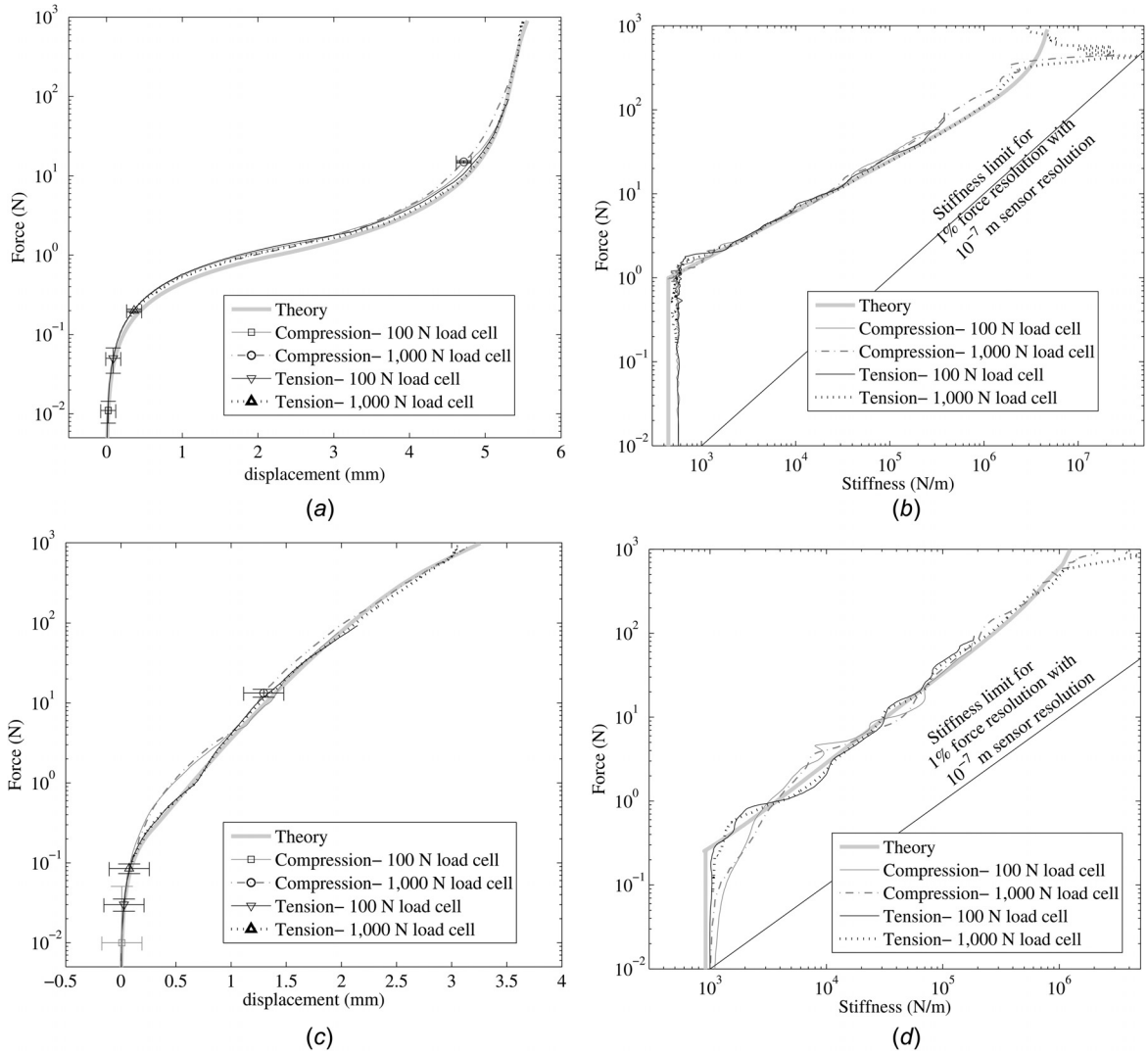

Fig. 4 Experimental force, stiffness, and deflection behavior for load cells shown in Figs. 2: (*a*) and (*b*) multipart load cell, (*c*) and (*d*) monolithic load cell. The horizontal and vertical bars indicate measurement uncertainty.

an Interface SM-25 load cell with a 100 N capacity for small forces, and an Interface SM-250 load cell with a 1000 N capacity for large forces. The nonlinear load cell bottom was bolted to the tabletop. The multipart nonlinear load cell top was bolted to the Interface load cell. A clevis pin attached to the Interface load cell went through a hole near the top of the monolithic nonlinear load cell.

We used spacer blocks to determine a reference point for the load cell zero deflection. For the multipart load cell, the zero-deflection point was determined by resting a spacer block on the bottom inner rigid block. The ADMET head traveled downward until the Interface load cell measured a sharp force increase to 5 N, which signified that the space between the top and bottom inner rigid blocks equaled the spacer block height of 17.3569 mm ± 0.0056 mm, based on micrometer measurements. Data from these procedures showed that the ADMET head traveled 0.0259 ± 0.0139 mm after the force started to abruptly increase.

For the monolithic load cell, the zero-deflection point was determined by resting two spacer blocks on the bottom inner rigid block. Due to gravity, the top inner block rested on the spacer blocks when the clevis pin, loose in the nonlinear load cell hole, was not supporting it. The ADMET head traveled upward until the Interface load cell measured an increased force of 0.1 N, signifying that the ADMET head was supporting the nonlinear load cell with a spacing between the inner and outer surfaces equal to the spacer block height. The spacer blocks had a height of 3.2310 ± 0.0036 mm, based on micrometer measurements.

During the tests, the ADMET head slipped at large forces. To account for this, we conducted force-versus-deflection tests in both tension and compression mode with the Interface load cell bolted directly to the bottom fixture to determine ADMET slip during the multipart load cell test and with the clevis pinned through a hole in a sufficiently rigid block ($\delta(P = 1000\,\mathrm{N}) \ll 0.001\mathrm{mm}$) to determine the ADMET slip during the monolithic load cell test. The mean experimental deflection from five trials was determined for each test configuration and direction. This deflection as a function of force was subtracted from the experimental nonlinear load cell deflection.

ADMET backlash and load cell taper contributed to an additional subtraction of 0.2095 ± 0.0890 mm from the deflection for the multipart load cell. ADMET backlash, clevis pin slip, and load cell taper contributed to an additional subtraction of 0.2193 ± 0.1745 mm from the deflection for the monolithic load cell.

The above sources of deflection uncertainty in the nonlinear load cell force-versus-displacement data include the spacer block height, the ADMET displacement resolution from both the

Table 2 Experimental deflection deviations

Experiment			Maximum error from theory		Maximum random deviation	
Load cell	Mode	Sensor load cell	Force (N)	Deflection dev. (%)	Force (N)	Deflection st. dev. (%)
Multipart	Compression	100 N	18	+28	0.011	30
Multipart	Compression	1000 N	39	+18	15	3.6
Multipart	Tension	100 N	0.011	+54	.011	150
Multipart	Tension	1000 N	428	+43	0.2	7.5
Monolithic	Compression	100 N	0.38	+91	0.01	396
Monolithic	Compression	1000 N	18	+46	13.3	13.3
Monolithic	Tension	100 N	0.011	+45	0.01	37
Monolithic	Tension	1000 N	7	+18	0.085	14

nonlinear load cell test and the ADMET slip tests, and the offset due to initial ADMET backlash, load cell taper, and slip. These sources sum to a zero-deflection point measurement uncertainty of ± 0.0948 mm for the multipart load cell and ± 0.1782 mm for the monolithic load cell, which are indicated by horizontal bars in Fig. 4. Deflection measurement relative to the zero-deflection point have ± 0.0001 mm uncertainty.

We performed five trials for both nonlinear load cells in both compression and tension modes, with a 100 N Interface load cell and a 1000 N Interface load cell and determined the experimental force mean and standard deviation as a function of load cell deflection.

As shown in Fig. 4, the force-versus-deflection experimental results generally agree well with the theory over the 0.01–1000 N range.

Table 2 lists the maximum experimental deflection deviations from the theory and standard deviations from random error for each experiment. The random errors at low range may be due to limited repeatability in the fixtures and limited precision in the sensor load cells used in our experiment. The errors from the theory may reflect the zero-deflection uncertainty due to the limited precision in the sensor load cells. The nonlinearity causes small deflection errors due to irrepeatability and imprecision to result in very large force errors from the theory as the force increases. Furthermore, as illustrated in Sec. 4, small fabrication errors in the surface shape may result in large force-versus-deflection errors. Fabricating the monolithic load cell root inserts too large may have caused the load cell to be stiffer than predicted for forces less than 13 N, which is when the ring contacts the root inserts.

Figures 4(*b*) and 4(*d*) show experimental stiffness curves that were determined by taking the gradient of the data moving average force and displacement in 0.05 mm segments. The waviness in these curves may reflect imprecision in the sensor load cell and repeatability issues, particularly with the monolithic load cell setup, as discussed in the previous paragraph for the force-versus-deflection plots. The additional waviness of the monolithic load cell compared to the multipart load cell may also be related to how the monolithic load cell has contact between two waterjetted surfaces, while the multi-part load cell has contact between a waterjetted surface and precision-ground spring steel.

We have assumed no-slip conditions in the ring as it contacts the surface. It is possible that large ring axial compression could violate the no-slip condition, in which case the contact point angle might be larger than expected, stiffening the actual behavior compared to the theory.

We have also assumed that transverse shear strain effects are negligible when we applied Euler–Bernoulli beam theory. Transverse shear strain effects are negligible when $t/\overline{R} < 0.1$ [19]. This condition holds along the entire length of the multipart load cell, for which $t/\overline{R} = 0.007$. This condition holds along 90% of the length of the monolithic ring, for which the thickness at $\theta_R = \pi/2$ leads to $t/\overline{R} = 0.13$. At 1000 N, the contact angle $\theta_{RC} = 1.0$ radians, and the root of the free length has $t/\overline{R} = 0.3$. Future work will extend the theory to include Timoshenko beam behavior that may become significant as the free length shortens and a larger fraction of the free length is thicker. Timoshenko beam behavior may be more important as we consider parameters that reduce the load cell size.

Despite the experimental errors from the theory, a nonlinear load cell product with a linear encoder deflection sensor may be calibrated so that it has high accuracy. The experimental stiffness versus force plots in Figs. 4(*b*) and 4(*d*) verify that both load cells have nonlinear stiffness curves below the maximum allowable stiffness for 1% force measurement resolution over the 0.01–1000 N range.

6 Conclusions

We showed how a load cell with increasing stiffness may be designed with a larger force measurement resolution and force range than a traditional linear load cell. We physically implemented a stiffening load cell by designing flexible rings that increasingly contact rigid surfaces as additional force is applied. As the ring contacts the rigid surfaces, two mechanisms stiffen the load cell: a shortening of the free ring segment's length and an increase in the free ring segment's average thickness (for the ring with a tapered thickness).

We investigated parameters that allow the nonlinear load cell to measure forces with resolutions of 1% of the applied force over a five-orders-of-magnitude force range, 0.01–1000 N. High resolution was achieved by designing the nonlinear load cell's stiffness to remain below values that allow a sensor with 0.1 μm resolution to detect changes larger than 1% the applied force.

We described methods for fabricating the load cell from multiple parts or from a monolithic part. The advantage of the waterjetted monolithic load cell is that its variable thickness ring allows for highly variable stiffness without large ring stresses. The advantage of the multipart load cell is that if the ring breaks, it may be replaced without replacing the entire load cell.

We experimentally verified the nonlinear load cell theory and showed the effectiveness of the fabrication method for the two different load cell designs.

The nonlinear load cell currently has several disadvantages compared to traditional linear load cells. If the ring thickness is large, then a large ring radius is required so that the initial load cell stiffness is low enough for ± 0.0001 N force resolution when 0.01 N is applied. With outer dimensions of $185 \times 170 \times 12.7$ mm^3 ($202 \times 200 \times 6.4$ mm^3), the multipart (monolithic) load cell is quite large compared to the $50 \times 60 \times 12$ mm^3 linear Interface load cells. The thin ring width, b, makes the load cell susceptible to out-of-plane parasitic motions. We found that the monolithic load cell had a very little resistance to out-of-plane bending, while the multipart load cell had more resistance due to the multipart load cell's larger ring width. The load cell requires a high-cost absolute linear encoder (on the order of $700) rather than a standard strain gauge (on the order of $30), because the absolute

deflection of the nonlinear load cell must be known in order to know the applied force.

Future work on this project will address these disadvantages and make other improvements:

- A thinner spring steel beam may allow a smaller load cell.
- A more costly but more accurate fabrication method such as wire electric discharge machining may also prove advantageous for decreasing load cell size.
- Surface curves of changing radii (such as ellipses) may reduce stress in the ring.
- Springs shaped with roll-annealed steel could eliminate prestress in the spring steel ring.
- A load cell manufactured with two or more well-spaced or perpendicular planes rather than a single plane may reduce sensitivity to out-of-plane parasitic loads.
- We will also add a linear encoder and test the functioning of the complete load cell.

While this paper focused on a 1% force resolution over 0.01–1000 N, the load cell design constraints may be adjusted for different ranges, resolutions, and sizes. Finally, we note that the design concepts described in this paper may apply to many other applications besides load cells.

Acknowledgment

We are grateful to Peter Liu for his assistance fabricating the load cells and to Wesley Cox for his assistance fabricating the load cells and performing experiments. The MicroMAX, named as the 2016 R&D 100 Finalist, was developed at OMAX under the support of an NSF SBIT Phase II grant. The research results in this manuscript are protected under patent US 9382960.

Funding Data

- Massachusetts Institute of Technology ("Efficient nonlinear energy harvesting from broad-band vibrational sources by mimicking turbulent energy transfer mechanisms" Project).
- National Science Foundation (Graduate Research Fellowship Program, 112237).

References

[1] Jung, D., and Gea, C., 2004, "Compliant Mechanism Design With Nonlinear Materials Using Topology Optimization," Int. J. Mech. Mater. Des., **1**(2), pp. 157–171.
[2] Thomas, M., 2012, "Design of Non-Serial, Non-Parallel Flexureal Transmissions as Applied to a Micro-Machined Mems Tuning Fork Gyroscope," Master's thesis, Massachusetts Institute of Technology, Cambridge, MA.
[3] Jeanneau, A., Herder, J., Laliberte, T., and Gosselin, C., 2004, "A Compliant Rolling Contact Joint and Its Application in a 3-DOF Planar Rolling Mechanism With Kinematic Analysis," ASME Paper No. DETC2004-57264.
[4] Teo, T., Chen, I., Yang, G., and Lin, W., 2008, "A Flexure-Based Electromagnetic Linear Actuator," Nanotechnology, **19**(31), p. 315501.
[5] Kluger, J., Sapsis, T., and Slocum, A., 2015, "Enhanced Energy Harvesting From Walking Vibrations by Means of Nonlinear Cantilever Beams," J. Sound Vib., **341**, pp. 174–194.
[6] Kluger, J., Sapsis, T., and Slocum, A., 2016, "A High-Resolution and Large Force-Range Load Cell by Means of Nonlinear Cantilever Beams," Precis. Eng., **43**, pp. 241–256.
[7] Smith, J., 2014, *Electronic Scale Basics*, Weighing and Measurement Publishing Company, Goodlettsville, TN.
[8] Sanders, J., Miller, R., Berglund, D., and Zachariah, S., 1997, "A Modular Six-Directional Force Sensor for Prosthetic Assessment: A Technical Note," J. Rehabil. Res. Dev., **34**(2), pp. 195–202.
[9] Mokhbery, J., 2006, "Advances in Load Cell Technology for Medical Applications," Medical Device and Diagnostic Industry Newsletter, Medical Device and Diagnostic Industry, accessed Aug. 14, 2014, http://www.mddionline.com/article/advances-load-cell-technology-medical-applications
[10] Change, Y.-S., and Lin, T.-C., 2013, "An Optimal G-Shaped Load Cell for Two-Range Loading," Eng. Agric., Environ., Food, **6**(4), pp. 172–176.
[11] Cordero, A., Carbone, G., Ceccarelli, M., Echavarri, J., and Munoz, J., 2014, "Experimental Tests in Human-Robot Collision Evaluation and Characterization of a New Safety Index for Robot Operation," Mech. Mach., Theory, **80**, pp. 184–199.
[12] Acuity, 2014, "Principles of Measurement Used by Laser Sensors," Acuity, Portland, OR, accessed July 29, 2017, https://www.acuitylaser.com/measurement-principles
[13] Lion, 2014, "Understanding Sensor Resolution Specifications and Effects on Performance," Lion, Oakdale, MN, Report No. LT05-0010.
[14] MTI, 2014, "Microtrak 3 Single Spot Laser Sensor," MTI Instruments, Albany, NY, Report No. m3_print.cdr 06122014.
[15] Storace, A., and Sette, P., 1977, "Leaf Spring Weighing Scale," Pitney-Bowes, Inc., Stamford, CT, U.S. Patent No. 4037675 A.
[16] Suzuki, S., Nishiyama, Y., and Kitagawa, T., 1987, "Multi-Range Load Cell Weighing Scale," Tokyo Electric Co., Ltd., Tokyo, Japan, U.S. Patent No. US 4711314 A.
[17] Kluger, J., Slocum, A., and Sapsis, T., 2016, "Beam-Based Nonlinear Spring," Massachusetts Institute of Technology, Cambridge, MA, U.S. Patent No. US 9382960 B2.
[18] Timoshenko, S., 1955, *Strength of Materials*, Van Nostrand, New York.
[19] Young, W. C., and Budynas, R. G., 2002, *Roark's Formulas for Stress and Strain*, McGraw-Hill, New York.
[20] Liu, P. H.-T., 2017, "Precision Machining of Advanced Materials With Waterjets," 5th Global Conference on Materials Science and Engineering (CMSE), Taiwan, China, Nov. 8–11.